Journal of Materials Chemistry A

PAPER

View Article Online
View Journal | View Issue

Cite this: J. Mater. Chem. A, 2017, 5, 14415

Novel Au/Cu_2O multi-shelled porous heterostructures for enhanced efficiency of photoelectrochemical water splitting†

Baoshun Wang,[a] Renying Li,[a] Zhiyun Zhang,[a] Weiwei Zhang,[b] Xiaolu Yan,[a] Xiaoling Wu,[ac] Guoan Cheng[ac] and Ruiting Zheng *[ac]

Received 14th March 2017
Accepted 13th June 2017

DOI: 10.1039/c7ta02254a

rsc.li/materials-a

In this study, we report novel Au/Cu_2O multi-shelled porous heterostructures (MSPHs). The results of photoelectrochemical (PEC) examination indicate that the photocurrent density of the as-prepared Au/Cu_2O MSPHs electrode reaches 150 μA cm^{-2}, which is almost 7.5 times higher than 20 μA cm^{-2} of pure Cu_2O MSP at a 0 V bias potential *versus* Ag/AgCl. The enhanced PEC efficiency of the Au/MSPHs is ascribed to the Schottky barrier at the Au–MSP NP interface and the surface plasmon resonance (SPR) effect of Au. We also found that Au nanoparticles deposited on the surface of Cu_2O MSP could effectively adjust their band structure.

1. Introduction

Cuprous oxide (Cu_2O) is a p-type oxide with a direct band gap of 2.0–2.2 eV.[1] It is an ideal photocathode material used in the photoelectrochemical (PEC) cell because the conduction band edge of Cu_2O is approximately 0.7 V negative than the hydrogen evolution potential. It makes direct generation of hydrogen at the photocathode surface possible.[2,3] However, the low migration rate of electrons and holes remains a bottleneck for its photocatalytic performance.

Recently, noble metal semiconductor heterostructures have drawn significant attention as photocatalysts. On the one hand, noble metal nanoparticles (NPs) are helpful for enhancing sunlight absorption through surface plasmon resonance (SPR) of noble metal NPs.[4,5] On the other hand, it is an efficient way to achieve higher separation efficiency of photoexcited electron–hole pairs and thus to obtain better photocatalytic performance.[6,7] Au and Ag are the frequently used metals for coupling onto semiconductors' surface.[8,9] Pan *et al.*[10] reported Au–Cu_2O nanowires in which the metallic Au NPs were deposited on the surface of Cu_2O nanowires. The presence of Au NPs can evidently enhance the photodegradation efficiency of Cu_2O. More recently, Zhang *et al.*[11] reported a heterostructure in which Au NPs of size 5–10 nm were deposited on the surfaces of Cu_2O microcubes. The photocurrent density of Au/Cu_2O heterostructures is 3 times than that of the pure Cu_2O microcubes.

In recent years, hollow micro-/nanostructures have attracted significant interest because of their unique properties such as low density, high specific surface area, and efficient paths for ion diffusion. These properties make them exhibit potential applications in photoelectrochemical water splitting.[12–17] As a specific hollow sub-microstructure, multi-shelled porous (MSP) spheres have larger specific surface areas and more deposition sites for metal NPs, which is an ideal material for PEC water splitting. Herein, we successfully prepared novel Au/Cu_2O MSP heterostructures by depositing monodispersed Au nanoparticles (NPs) of size 3–5 nm on the external and internal surfaces of the Cu_2O multi-shelled porous (MSP) sub-micron spheres. The photocurrent density of the as-prepared Au/Cu_2O heterostructure electrode reaches 150 μA cm^{-2} under sunlight (AM 1.5G) irradiation, which is almost 7.5 times higher than that of pure Cu_2O MSP electrode (20 μA cm^{-2}) at a bias potential of 0 V *versus* Ag/AgCl. To the best of our knowledge, it is the highest photocurrent density for metal/Cu_2O heterogeneous materials without bias potential. The mechanism for the enhanced PEC efficiency in the Au/MSP heterostructures (MSPHs) has been discussed in detail.

2. Experimental

2.1 Chemicals

Copper(II) sulfate pentahydrate ($CuSO_4 \cdot 5H_2O$, 99%) and sodium citrate ($C_6H_5Na_3O_7 \cdot 2H_2O$) were purchased from Xilong Chemical Co. Hexadecyltrimethylammonium bromide ($C_{19}H_{42}BrN$, 99%), ascorbic acid ($C_6H_8O_6$, 99.7%), and hydrogen tetrachloroaurate trihydrate ($HAuCl_4 \cdot 3H_2O$, 99%) were purchased from Sinopharm Chemical Reagent Co. Sodium

[a]Key Laboratory of Radiation Beam Technology and Materials Modification of Ministry of Education, College of Nuclear Science and Technology, Beijing Normal University, Beijing 100875, P. R. China. E-mail: rtzheng@bnu.edu.cn

[b]School of Science, Minzu University of China, Beijing 10081, PR China

[c]Beijing Radiation Center, Beijing 100875, P. R. China

† Electronic supplementary information (ESI) available. See DOI: 10.1039/c7ta02254a

hydroxide (NaOH, 98%) was purchased from Beijing Chemical Works. DI water was prepared in our lab.

2.2 Fabrication of the Au/Cu_2O MSPHs

Cu_2O MSP sub-micron spheres were synthesized by a liquid chemical method, which was described in our previous study.[15] The Au/Cu_2O MSPHs were fabricated by a facile chemical route at room temperature. First, 10 mg of the as-prepared Cu_2O MSP sub-micron spheres were distributed in 20 mL water and alcohol mixed solution (volume ratio 1 : 1) *via* magnetic stirring. Then, 1.5 mL of 0.05 M sodium citrate ($C_6H_5Na_3O_7 \cdot 2H_2O$) solution was added, and the mixed solution was sonicated in a water bath at 70 Hz for 10 min. Finally, the mixed solution was moved to a darkroom, and 0.03 mL of 0.049 M chloroauric acid ($HAuCl_4$) solution was injected into the mixed solution. After 20 minutes of reaction under vigorous stirring, the solution changes from dark yellow to breen. The precipitates were separated by centrifugation and sequentially washed three times with de-ionized water and ethanol. After drying in a 60 °C vacuum oven for 5 h, the Au/Cu_2O MSP heterostructure powder was obtained.

2.3 Fabrication of the Au NPs

First, 147 mg of sodium citrate ($C_6H_5Na_3O_7 \cdot 2H_2O$) was placed in a beaker with 10 mL de-ionized water, followed by vigorous stirring to obtain solution A. Then, the solution A was moved to a darkroom, and 0.18 mL of 0.049 M chloroauric acid ($HAuCl_4$) solution was injected into solution A under vigorous stirring. After 20 minutes of reaction, the precipitates were separated by centrifugation, sequentially washed three times with de-ionized water and ethanol, and dried in a 60 °C vacuum oven for 5 h. Finally, black Au NPs were obtained.

2.4 Structural characterization

The chemical structure and components of the as-prepared products were identified by X-ray diffraction (XRD, Bruker D8 Advance diffractometer) with Cu Kα radiation ($\lambda = 0.1506$ nm). The morphology and size of the products were observed by scanning electron microscopy (SEM, HITACHI S-4800). Transmission electron microscopy (TEM) and high-resolution TEM (HRTEM) images were obtained *via* a F20 transmission electron microscope. Room temperature UV-vis diffuse reflectance spectra (DRS) were obtained using a Perkin Elmer Lambda 950 UV-vis-NIR spectrophotometer (Perkin-Elmer, USA). The surface electronic states of the products were determined by X-ray photoelectron spectroscopy (XPS, ESCALAB 250Xi, UK).

2.5 Photocurrent measurements

Herein, 5 mg of the as-prepared Cu_2O or Au/Cu_2O powder was dispersed in 100 μL ethanol to form a stable suspension. Then, the suspension was placed on a piece of FTO glass (1.5 × 3.0 cm^2, 10 Ω cm^{-1}) and dried using a 60 °C thermostat to make a film electrode. Copper wires were used to connect the film electrodes. The areas of the film electrodes were about 1 cm^2. Photocurrent measurements were carried out using a bipotentiostat (Model AFCBP1, USA) in the dark. The light source employed in the PEC studies was a 300 W xenon lamp with an AM 1.5G filter (MAX-302, Asahi Spectra, USA). For all the measurements, a three-electrode system was used. A platinum line was used as a counter electrode, and Ag/AgCl (in a 3.0 M KCl solution) was used as a reference electrode. The electrolyte was 0.5 M Na_2SO_4 electrolyte solution (pH = 7) deaerated by bubbling N_2 for at least 25 min before each experiment.

3. Results

3.1 Microstructure of the MSP and Au/MSPHs

Fig. 1 shows the morphologies and microstructures of the as-prepared pure MSP and Au/MSPHs determined *via* TEM. The average diameter of MSP is about 150–200 nm, and the average diameter of the pores on the sphere surface is about 30 nm, as shown in Fig. 1(A). Moreover, it can be clearly observed that the surfaces of the MSP are smooth. After coating Au on the surface of MSP by a facile chemical route, we found some monodispersed NPs on the surface of MSP, as shown in Fig. 1(B). The average diameter of NPs is about 3–5 nm. Fig. S1 (see the ESI†) shows the typical XRD pattern of the as-prepared MSP and Au/MSPHs. The XRD pattern of MSP can be perfectly indexed to cubic Cu_2O (JCPDS file no. 65-3288). After coating the Au NPs, the XRD pattern was found to be similar to that of MSP. Only one very weak diffraction peak at 38.18° appeared. This peak can be indexed to the (111) crystal plane of the cubic Au crystal (JCPDS file no. 89-3697). The relatively weak diffraction peak of the Au NPs indicated the low content of Au as compared to that of Cu_2O.

The HRTEM image of the Au/MSPHs is presented in Fig. 1(C), which is obtained near the surface of the MSP. HRTEM image reveals distinct lattice fringes with the *d* spacing of 0.211 nm and 0.244 nm in MSP, which corresponds to the (200) and (111) planes of Cu_2O, respectively. The lattice with the distance of 0.233 nm and 0.205 nm in the surface particle should be the (111) and (200) planes of Au. The (200) and (111) planes of Cu_2O match well with the corresponding planes of Au; it reveals that the Au NPs directly grow on the surface of the MSP. The TEM-EDS mappings of the as-prepared Au/MSP nanostructures are shown in Fig. 1(D)–(G). Fig. 1(D) clearly indicates that the composite nanoparticle is a core–shell structure. The O and Cu elements have similar distributions, as shown in Fig. 1(E) and (F), respectively. However, Au dots uniformly distribute within the projected area of the Au/MSP nanostructures; this reveals that Au particles are uniformly deposited on the external and internal surfaces of the MSP microspheres to construct multidimensional heterostructures, as shown in Fig. 1(G).

Fig. 1(H) is the fine-scan XPS spectrum of Cu 2p, where there are two peaks at the binding energies of 932.6 and 952.5 eV. These two peaks can be assigned to Cu^+ $2p_{3/2}$ and $2p_{1/2}$, indicating the presence of Cu_2O.[18] Fig. 1(I) is the fine-scan XPS spectrum of Au 4f. The two peaks located at 84.33 and 88.03 eV can be assigned to Au $4f_{7/2}$ and Au $4f_{5/2}$, respectively, both of which are attributed to Au (0).[19] The XPS spectrum further confirms the existence of Au (0) NPs on the MSP microspheres.

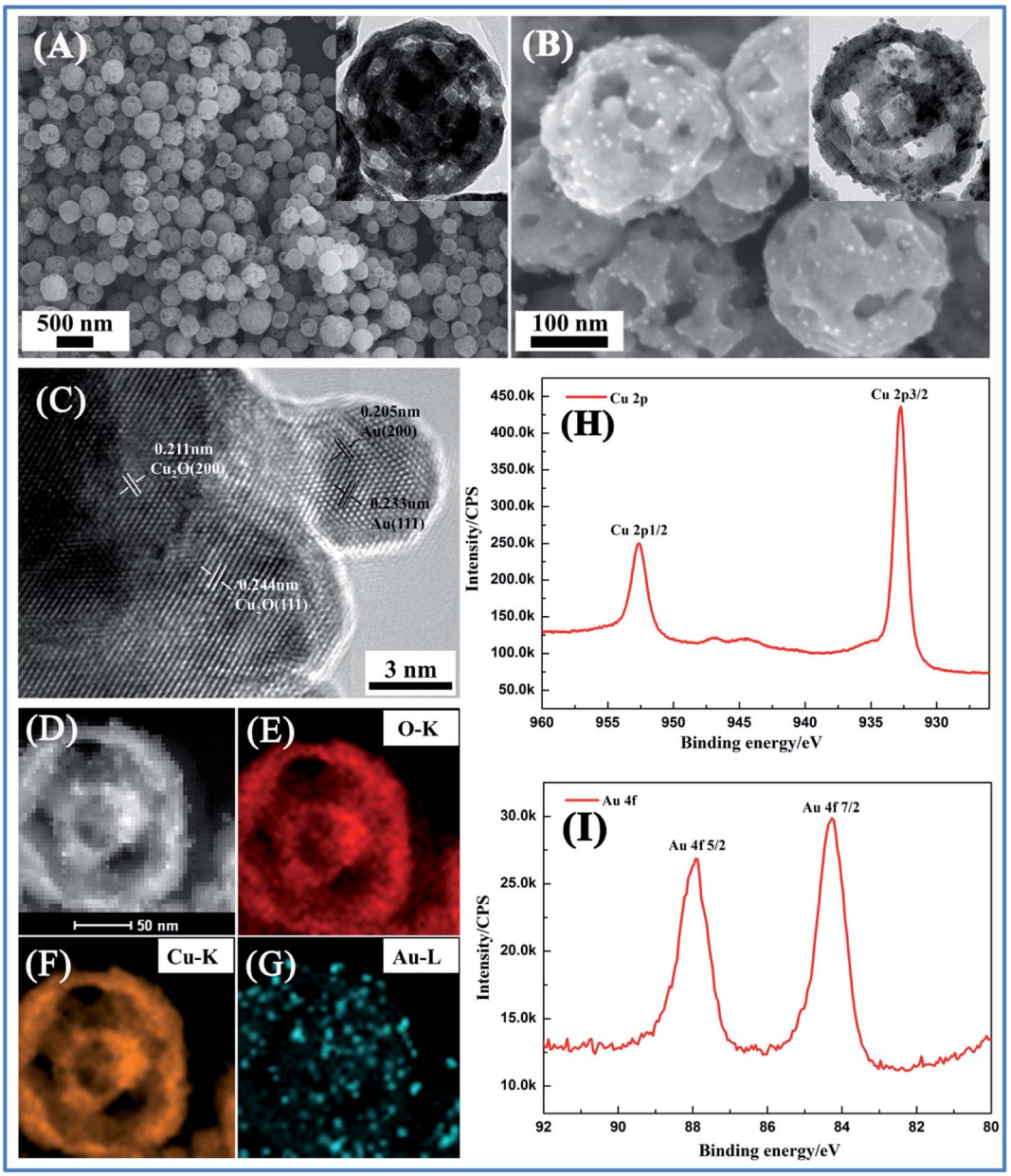

Fig. 1 (A) and (B) SEM images of MSP and Au/MSPHs (the insets are the TEM images of MSP and Au/MSPHs). (C) The corresponding HRTEM image of the Au/MSPHs. (D)–(G) TEM-EDS mappings and the corresponding elemental mapping of Au/MSPHs. (H) XPS spectrum survey of Cu 2p band. (I) XPS spectrum survey of the Au 4f band.

3.2 Optical properties

We also prepared monodispersed Au NPs with the size of 30–50 nm by the method abovementioned in the experimental section, as shown in Fig. S2 (see the ESI†). As is well known, Au NPs exhibit strong surface plasmon resonance (SPR) effects owing to the collective oscillation of the conduction electrons when the Au NPs are exposed to an external electromagnetic field.[20] Fig. 2 shows the UV-vis diffuse reflectance spectra (DRS) of the as-prepared MSP, monodispersed Au NPs, and Au/MSPHs. The SPR effect enables Au NPs to have a broad absorption range from 550 to 800 nm (indicated by a blue line in Fig. 2). The spectrum of MSPs shows broad absorption ranging from 400 to 500 nm (indicated by a black line in Fig. 2). The broad absorption of MSP is attributed to the intrinsic absorption of Cu_2O and the porous nanostructure of MSP. However, the light absorption of MSP reduces rapidly beyond 600 nm because Cu_2O MSP is almost transparent for the photons with the energy below 2 eV. After coating Au NPs on MSP, Au/MSPHs exhibit a broad absorption in all visible light regions (as indicated by a red line in Fig. 2). By comparing the UV-vis absorption spectra of Au NPs and Cu_2O MSP, it was observed that the strong light absorption between 400 and 500 nm was mainly due to Cu_2O MSP. In addition, light absorption beyond 600 nm should be due to Au nanoparticles. According to a previous report, when Au NPs are adsorbed on the surface of the

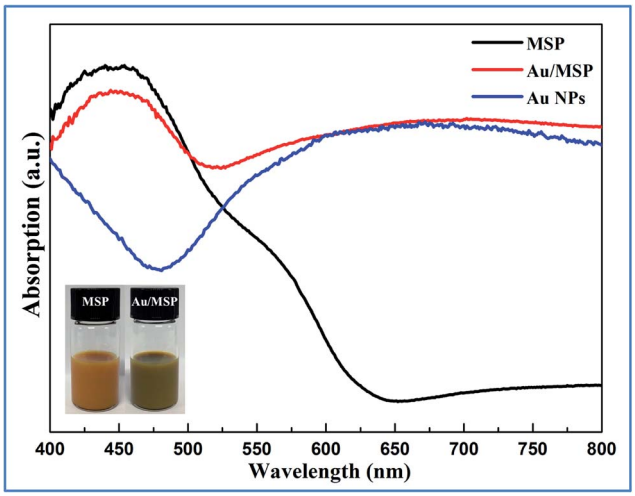

Fig. 2 UV-vis diffuse reflectance spectra (DRS) of the as-prepared MSP, Au/MSPHs, and Au NPs. Inset: images showing the color of the solution of MSP and Au/MSPHs.

nanocrystals, strong surface-enhanced Raman scattering (SERS) effects can be observed.[21] Although we did not know if we could further improve the light absorption using smaller MSP, we proved that the light absorption in the whole visible light region could be improved by combining Cu_2O MSP and Au NPs. MSPHs successfully construct a multidimensional structure to build up more SPR active sites, which is important to broaden the light absorption region.

3.3 PEC properties

To evaluate the PEC activity of the as-prepared samples, photocurrent was measured in a three-electrode cell, with Ag/AgCl as the reference electrode, Pt wire as the counter electrode, and the as-prepared samples as the working electrode. Fig. 3 shows the photoelectrochemical response of the as-prepared samples. We can see that the photocurrent density

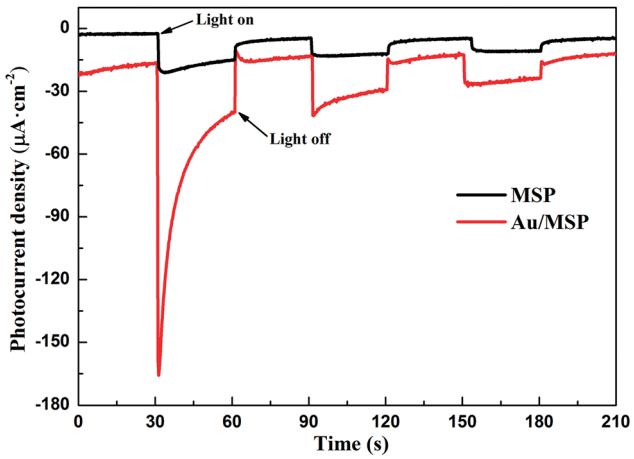

Fig. 3 Photocurrent density–time characteristics in 0.5 M Na_2SO_4 solution, under AM 1.5G light illumination for the MSP and Au/MSPH electrode at 0 V *versus* Ag/AgCl with N_2 purging.

of the Cu_2O MSP is about 20 μA cm^{-2} in the first cycle. With the increase in the illumination time, the photocurrent densities gradually decreased. The photocurrent densities are finally stabilized at around 10 μA cm^{-2}. There are two common reasons account for photocurrent decreased. One is high photogenerated charge recombination rate of pristine Cu_2O.[11,22] The other reason is photocorrosion caused by photoinduced electrons.[2–23] However, the as-fabricated Au/Cu_2O MSPHs exhibited better PEC performance than the pristine Cu_2O MSP. In the first light impulse, the photocurrent density of the Au/Cu_2O MSPHs electrode reaches 150 μA cm^{-2}, which is almost 7.5 times higher than that of Cu_2O MSP (20 μA cm^{-2}). To the best of our knowledge, under the condition of no bias potential, this photocurrent value is highest in the existing reports on the use of Au/Cu_2O heterostructures as a photoelectrode for water splitting.[24–26] The photocurrent densities of other Cu_2O or Au/Cu_2O powder electrodes are listed in Table S1 (see the ESI†). As is known, photoinduced cathodic current reveals the generation and separation dynamics of photogenerated charges in the semiconductor photocatalysts. Without bias potential, the photocurrent directly reflects the photogeneration charge separation efficiency at the Au/MSP interfaces.[27,28] Higher photocurrent means better photogeneration charge separation efficiency.

We found that the photocurrent gradually decreased. There are two common reasons for Cu_2O or Au/Cu_2O. Photocorrosion is considered to be the first reason. Because the redox potentials for the reduction and oxidation of Cu_2O lie between the band gap of the hydrogen evolution potential and the oxygen evolution potential. When Cu_2O is irradiated by visible light, the following two reactions (eqn (1) and (2)) occur. Cu_2O will be corroded into CuO and Cu during the process of water splitting.[2,29,30]

$$Cu_2O + H_2O + 2e^- \rightarrow 2Cu + 2OH^- \quad (1)$$

$$Cu_2O + 2OH^- \rightarrow 2CuO + H_2O + 2e^- \quad (2)$$

However, as shown in Fig. S3,† the microstructures of the as-prepared Au/MSP and those obtained after water splitting can be observed. The microstructures of the Au/Cu_2O MSPs have no obvious change. Moreover, the XPS spectrum of the Au/MSP after water splitting is shown in Fig. S4.† There is no obvious change in the XPS spectrum of the sample after water splitting. Therefore, photocorrosion may not be the main reason for photocurrent decrease in Au/MSP. Another important reason cannot be ignored: the working electrode was made by coating the Cu_2O or Au/Cu_2O suspension on FTO, and no adhesive was adopted. When the working electrode was immersed in the electrolyte, liquid environment weakened the contact between the sample and FTO as time passed, thereby increasing the contact resistance between Cu_2O or Au/Cu_2O powder and FTO.[31,32]

Moreover, we found that photocurrent density obviously decreased on the Au/Cu_2O MSP electrode in the first impulse. We believe that the important reason for the first photocurrent density peak of Au/Cu_2O MSP electrode is the existence of the Au/Cu_2O Schottky barrier. With the help of the Schottky barrier, the photoinduced electron–hole pairs in Au/MSP can be more

effectively separated than those in pure Cu_2O MSP; thus, Au/MSP has a larger photocurrent density in the first cycle. However, with the increase in the illumination time, the photocurrent densities quickly decreased. The main reason is that more and more electrons move from Cu_2O to Au NPs under the inner electric field between Au and Cu_2O. However, as the Au NPs are monodispersed on Cu_2O, the electrons on the surface of Au NPs cannot transport in time. A number of electrons will accumulate on the surface of the Au NPs and the inner electric fields between Au and Cu_2O become weak. As a result, the photoinduced electron–hole pairs cannot be effectively separated at the beginning of the experiment. Hence, the photocurrent densities of Au/MSP decrease, but it is still higher than that of pure Cu_2O. Therefore, the first cycle is more representative of the photoelectrochemical properties of the materials.

4. Discussion

It has been reported that when a p-type semiconductor contacts a metal and their work functions satisfy the criteria $W_s > W_m$ (where W_s and W_m are the work functions of the semiconductor and metal, respectively), a Schottky junction can be built at the interface of the semiconductor and the metal, which will drive the electrons to transfer from the metal to the semiconductor.[33] The approximate work functions of Au and Cu_2O are 5.10 and 5.27 eV, respectively. When Au NPs are deposited on the surface of Cu_2O MSP, electrons will transfer from Au to Cu_2O until thermodynamic equilibrium is established, as shown in Fig. 4(a). As a result, an inner electric field between Au and Cu_2O is established. Moreover, the Femi level of Au will be descended, and the Femi level of Cu_2O will be raised up. The energy band at the Au/Cu_2O interface is curved, and the conduction band (CB) edge of Cu_2O is higher than the Femi level of the thermodynamic equilibrium state, as shown in Fig. 4(b).

When Au/MSP nanostructures are excited by light irradiation, photoinduced electron–hole pairs are generated; the electrons in the CB of MSP migrate to Au NPs with the help of the inner electric field, whereas the electrons in the Au NPs cannot be transferred to Cu_2O due to the Schottky barrier. Therefore, the photoinduced electron–hole pairs can be effectively separated. Then, the photoinduced holes on the VB migrate from FTO to the counter electrode to react with H_2O to produce O_2, whereas the electrons immediately react with H^+ to produce H_2. The possible PEC reaction of the Au/MSP nanostructures in water can be proposed as follows (eqn (3)–(6)):

$$Au \rightarrow Au^+ + e^- \quad (3)$$

$$Cu_2O + h\nu \rightarrow h^+ + e^- \quad (4)$$

$$2H^+ + 2e^- \rightarrow H_2 \quad (5)$$

$$2H_2O + 4h^+ \rightarrow O_2 + 4H^+ \quad (6)$$

To further illustrate the band alignment of Cu_2O and Au/Cu_2O, their Fermi energy (E_f) and work functions (Φ) are

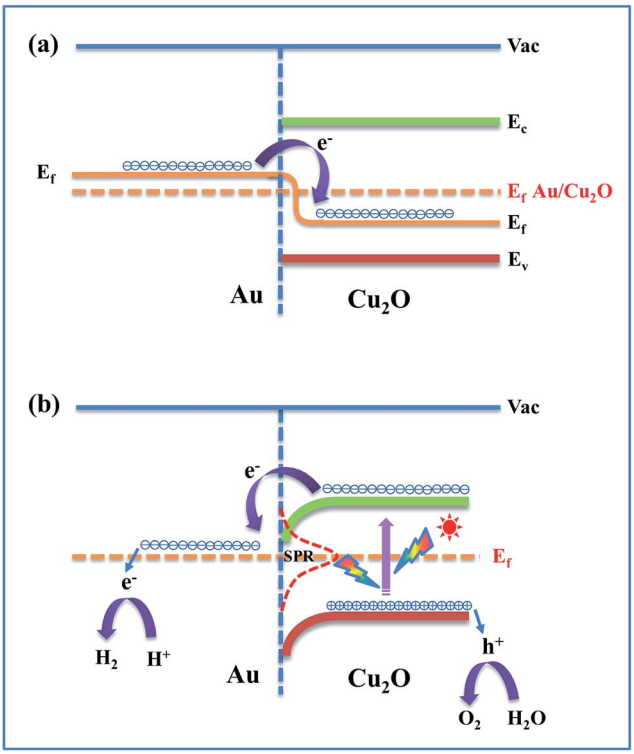

Fig. 4 Schematic of (a) an inner electric field formation process between Au and Cu_2O, (b) the charge separation process and photocatalytic mechanism of the Au/MSPHs under AM 1.5G irradiation. Herein, E_f is the Fermi energy level, CB is the conduction band, and VB is the valence band. All these values are for standard conditions; however, under the experimental conditions, these values may vary slightly.

measured by ultraviolet photoelectron spectroscopy (UPS), as shown in Fig. S5.† The cut-off energy (E_{cutoff}) and E_f are determined by linear extrapolation of the profiles to zero. As shown in Fig. S3,† E_f values of MSP and Au/MSP are 4.79 eV and 4.88 eV, respectively. It can be seen that when Au NPs are coated on the Cu_2O MSP, the Fermi energy of Cu_2O MSP is elevated. Therefore, the UPS result also confirmed that Au NPs indeed change the band structure of Cu_2O MSP.

The work functions (Φ) of the materials can be calculated according to the UPS data using eqn (7):

$$\Phi = h\nu - E_{cutoff} + E_f \quad (7)$$

where $h\nu$ (=21.22 eV) is the incoming photon energy from the He I source. The E_{cutoff} values of MSP and Au/MSP are 20.70 eV and 21.24 eV, respectively. The E_f values of MSP and Au/MSP are 4.79 eV and 4.88 eV, respectively. The calculated work functions of MSP and Au/MSP are 5.31 eV and 4.86 eV, respectively. The Au/MSP showed lower work functions, which means that Au/MSP easily produces photogenerated carrier than pure MSP under the same conditions. It has also been proved that Au/MSP has better photocatalytic performance.

The effect of inner electronic field and the Schottky barrier at the Cu_2O/Au interface could be further proved by electrochemical impedance spectroscopy (EIS). It is known that the

semicircle in the Nyquist plot at high frequencies is the characteristic of the charge transfer process, and the diameter of the semicircle is equal to the charge transfer resistance (R_{ct}).[34–36] As shown in Fig. 5, electrochemical impedance spectroscopy (EIS) of MSP and Au/MSPHs was carried out under illumination in 0.5 M Na_2SO_4 at a bias potential of 0 V *vs.* Ag/AgCl. It can be easily observed that the R_{ct} of Au/MSPHs was apparently smaller than that of the pristine MSP under AM 1.5G irradiation (~100 Ω *vs.* ~2500 Ω). This result indicates that Au/MSPHs dramatically promoted the interfacial charge transport and the separation efficiency of the photoinduced charges with the help of inner electronic field and the Schottky barrier and further enhanced the PEC performance.

Moreover, we also carried out the photoluminescence (PL) measurement of the Cu_2O MSP and Au/Cu_2O MSP under an excitation wavelength of 325 nm, as presented in Fig. S6.† Au/Cu_2O MSP shows a relatively low PL intensity than Cu_2O MSP, which indicates that the mitigated charge recombination rate in Au/Cu_2O MSP is lower than that in Cu_2O MSP.[37] The reason should be the Au/Cu_2O Schottky barrier, which improves the separation efficiency of the light-stimulated carriers.

For a crystalline semiconductor, its band gap can be obtained from the corresponding modified Kubelka–Munk function through the UV-vis diffuse reflectance spectra.[38,39] The band gap energies (E_g values) of MSP and Au/MSPHs were estimated by the classical Tauc approach, as shown in Fig. 6. The absorption edge energies of MSP and Au/MSPHs were obtained by the intercept of the tangent to *X*-axis at $F = 0$. The estimated band gap energies of MSP and Au/MSPHs were 2.28 eV and 2.17 eV, respectively. The band gap of Au/MSPHs is slightly lower than that of MSP, which is in agreement with its stronger light absorption, as shown in Fig. 2. Moreover, this result also proves that Au NPs deposited on the surface of Cu_2O MSP can adjust its band structure, as shown in Fig. 4. Smaller E_g makes Au/MSP have larger absorption range and harvest more solar energy, which is beneficial for generating more electron–hole pairs to join in the redox reaction and producing bigger photocurrent.

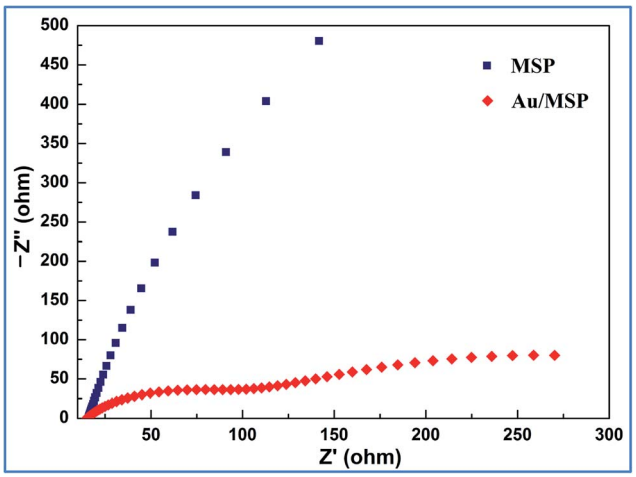

Fig. 5 EIS Nyquist plots of the pristine MSP and Au/MSPHs under AM 1.5G illumination in 0.5 M Na_2SO_4 at a bias potential of 0 V *vs.* Ag/AgCl.

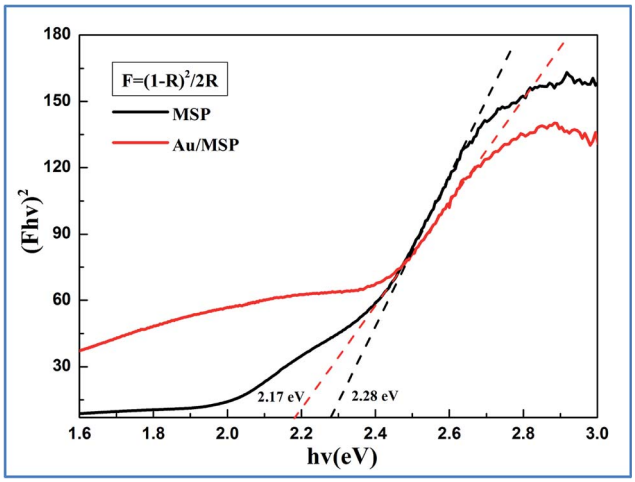

Fig. 6 The term $(Fh\nu)^2$ is a function of photon energy ($h\nu$), where *F* is the Kubelka–Munk function of the diffuse reflectance *R* from Ultraviolet-visible diffuse reflectance spectra. The intercepts of the extrapolated straight lines give the corresponding direct band gaps of MSP and Au/MSPHs.

5. Conclusions

In summary, we successfully designed novel Au/Cu_2O MSPHs. This multi-dimensional composite structure exhibits superior PEC performance. The experimental results indicate that the as-fabricated Au/MSPHs have smaller R_{ct} and lower work functions and PL intensity than pristine MSP. The photocurrent density of the as-prepared Au/Cu_2O MSPH electrode reaches up to 150 μA cm^{-2}, which is almost 7.5 times higher than that of pure Cu_2O MSP (20 μA cm^{-2}) at a bias potential of 0 V *versus* Ag/AgCl. The enhanced PEC efficiency of the Au/MSPHs is ascribed to their novel structure. The multi-shelled porous structure of the Cu_2O particles makes them have higher specific surface area. Enormous Au nanoparticles deposited on the semiconductor surface can act as electron sinks, which provide sites for the accumulation of the photoinduced electrons and then improve the separation efficiency of the photoinduced electron–hole pairs. Furthermore, Au NPs exhibit strong SPR effect and effectively decrease the E_g of the Cu_2O MSP, which is useful to enhance the light absorption. More light absorption will produce more carriers to obtain better PEC activity. This study not only provides high-efficiency Au/Cu_2O PEC material, but also provides a new idea to build multi-dimensional composite structures in designing photoactive materials.

Acknowledgements

This work was supported by the National Natural Science Foundation of China (11575025) and the Fundamental research Funds for the Central Universities.

References

1 P. E. de Jongh, D. Vanmaekelbergh and J. J. Kelly, *J. Electrochem. Soc.*, 2000, **147**, 486–489.

2 A. Paracchino, V. Laporte, K. Sivula, M. Grätzel and E. Thimsen, *Nat. Mater.*, 2011, **10**, 456–461.
3 J. Y. Zheng, G. Song, C. W. Kim and Y. S. Kang, *Electrochim. Acta*, 2012, **69**, 340–344.
4 S. R. Zhang, R. B. Jiang, Y. Z. Guo, B. C. Yang, X. L. Chen, J. F. Wang and Y. F. Zhao, *Small*, 2016, **31**, 4264–4276.
5 H. J. Wang, K. H. Yang, S. C. Hsu and M. H. Huang, *Nanoscale*, 2016, **8**, 965–972.
6 M. A. Mahmoud, W. Qian and M. A. El-Sayed, *Nano Lett.*, 2011, **11**, 3285–3289.
7 Z. H. Wang, S. P. Zhao, S. Y. Zhu, Y. L. Sun and M. Fang, *CrystEngComm*, 2011, **13**, 2262–2267.
8 Y. H. Zheng, C. Q. Chen, Y. Y. Zhan, X. Y. Lin, Q. Zheng, K. M. Wei and J. F. Zhu, *J. Phys. Chem. C*, 2008, **112**, 10773–10777.
9 L. Zhang, H. Jing, G. Boisvert, J. Z. He and H. Wang, *ACS Nano*, 2012, **6**, 3514–3527.
10 Y. L. Pan, S. Z. Deng, L. Polavarapu, N. Y. Gao, P. Y. Yuan, C. H. Sow and Q. H. Xu, *Langmuir*, 2012, **28**, 12304–12310.
11 W. W. Zhang, B. S. Wang, C. C. Hao, Y. J. Liang, H. L. Shi, L. Ao and W. Z. Wang, *J. Alloys Compd.*, 2016, **684**, 445–452.
12 Z. Wang, J. G. Hou, C. Yang, S. Q. Jiao, K. Huang and H. M. Zhu, *Energy Environ. Sci.*, 2013, **6**, 2134–2144.
13 J. Zhao, Y. C. Zou, X. X. Zou, T. Y. Bai, Y. P. Liu, R. Q. Gao, D. J. Wang and G. D. Li, *Nanoscale*, 2014, **6**, 7255–7262.
14 L. Zhang, H. B. Wu, Y. Yan, X. Wang and X. W. Lou, *Energy Environ. Sci.*, 2014, **7**, 3302–3306.
15 B. S. Wang, W. W. Zhang, Z. Y. Zhang, R. Y. Li, Y. L. Wu, Z. G. Hu, X. L. Wu, C. G. Guo, G. A. Cheng and R. T. Zheng, *RSC Adv.*, 2016, **6**, 103700–103706.
16 J. H. Sohn, H. G. Cha, C. W. Kim, D. K. Kim and Y. S. Kang, *Nanoscale*, 2013, **5**, 11227–11233.
17 C. W. Kim, S. P. Suh, M. J. Choi, Y. S. Kang and Y. S. Kang, *J. Mater. Chem. A*, 2013, **1**, 11820–11827.
18 C. K. Wu, M. Yin, S. O'Brien and J. T. Koberstein, *Chem. Mater.*, 2016, **18**, 6054–6058.
19 W. L. Cheng, S. J. Dong and E. Wang, *Langmuir*, 2003, **19**, 9434–9439.
20 M. L. Pang, Q. X. Wang and H. C. Zeng, *Chem.–Eur. J.*, 2012, **18**, 14605–14609.
21 D. F. Zhang, L. Y. Niu, L. Jiang, P. G. Yin, L. D. Sun, H. Zhang, R. Zhang, L. Guo and C. H. Yan, *J. Phys. Chem. C*, 2008, **112**, 16011–16016.
22 J. H. Yang, D. E. Wang, H. X. Han and C. Li, *Acc. Chem. Res.*, 2013, **46**, 1900–1909.
23 J. Y. Zheng, T. K. Van, A. U. Pawar, C. W. Kim and Y. S. Kang, *RSC Adv.*, 2014, **4**, 18616–18620.
24 C. J. Engel, T. A. Polson, J. R. Spado, J. M. Bell and A. Fillinger, *J. Electrochem. Soc.*, 2008, **155**, 37–42.
25 Z. Yang, C. K. Chiang and H. T. Chang, *Nanotechnology*, 2008, **19**, 025604–025610.
26 Y. F. Zhao, Z. Y. Yang, Y. X. Zhang, L. Jing, X. Guo, Z. T. Ke, P. W. Hu, G. X. Wang, Y. M. Yan and K. N. Sun, *J. Phys. Chem. C*, 2014, **118**, 14238–14245.
27 Y. K. Hsua, C. H. Yua, Y. C. Chen and Y. G. Lin, *Electrochim. Acta*, 2013, **105**, 62–68.
28 Y. M. He, J. Cai, T. T. Li, Y. Wu, H. J. Lin, L. H. Zhao and M. F. Luo, *Chem. Eng. J.*, 2013, **215**, 721–730.
29 W. Siripala, A. Ivanovskaya, T. F. Jaramillo, S. H. Baeck and E. W. McFarland, *Sol. Energy Mater. Sol. Cells*, 2003, **77**, 229–237.
30 B. P. Rai, *Solar Cells*, 1988, **25**, 265–272.
31 J. Y. Zheng, G. Song, C. W. Kim and Y. S. Kang, *Nanoscale*, 2013, **5**, 5279–5282.
32 Y. S. Kang, S. Risbud, J. Rabolt and P. Stroeve, *Langmuir*, 1996, **12**, 4345–4349.
33 L. L. Wang, J. Ge, A. L. Wang, M. S. Deng, X. J. Wang, S. Bai, R. Li, J. Jiang, Q. Zhang, Y. Luo and Y. J. Xiong, *Angew. Chem.*, 2014, **126**, 5207–5211.
34 Z. Kang, X. Q. Yan, Y. F. Wang, Z. M. Bai, Y. C. Liu, Z. Zhang, P. Lin, X. H. Zhang, H. G. Yuan, X. J. Zhang and Y. Zhang, *Sci. Rep.*, 2014, **5**, 7882–7889.
35 W. W. Zhou, J. X. Zhu, C. W. Cheng, J. P. Liu, H. P. Yang, C. X. Cong, C. Guan, X. T. Jia, H. J. Fan, Q. Y. Yan, C. M. Li and T. Yu, *Energy Environ. Sci.*, 2011, **4**, 4954–4961.
36 J. Y. Zheng, G. Song, J. Hong, T. K. Van, A. U. Pawar, D. Y. Kim, C. W. Kim, Z. Haider and Y. S. Kang, *Cryst. Growth Des.*, 2014, **14**, 6057–6066.
37 G. Katsukis, J. Malig, C. S. Drost, S. Leubner, N. Jux and D. M. Guldi, *ACS Nano*, 2012, **6**, 1915–1924.
38 T. J. McCarthy, T. A. Tanzer and M. G. Kanatzidis, *J. Am. Chem. Soc.*, 1995, **117**, 1294–1301.
39 G. W. Zhou and Y. S. Kang, *Mater. Sci. Eng., C*, 2004, **24**, 71–74.